

See discussions, stats, and author profiles for this publication at: <https://www.researchgate.net/publication/46271688>

Grazing Incidence Small Angle X-ray Scattering on Colloidal Crystals

ARTICLE *in* THE JOURNAL OF PHYSICAL CHEMISTRY B · OCTOBER 2010

Impact Factor: 3.3 · DOI: 10.1021/jp103943y · Source: PubMed

CITATIONS

3

READS

27

5 AUTHORS, INCLUDING:



Ullrich Pietsch

Universität Siegen

412 PUBLICATIONS 3,733 CITATIONS

SEE PROFILE



Marcus Textor

ETH Zurich

333 PUBLICATIONS 14,002 CITATIONS

SEE PROFILE

Grazing Incidence Small Angle X-ray Scattering on Colloidal Crystals

Patrick Huber,[†] Oliver Bunk,[‡] Ullrich Pietsch,[§] Marcus Textor,[⊥] and Thomas Geue^{†,*}

Laboratory for Neutron Scattering, ETH Zurich and Paul Scherrer Institut, 5232 Villigen PSI, Switzerland, Research Department of Synchrotron Radiation and Nanotechnology, Paul Scherrer Institute, 5232 Villigen PSI, Switzerland, Solid State Physics Group, University of Siegen, 57068 Siegen, Germany and Laboratory for Surface Science and Technology, ETH Zurich, 8093 Zürich, Switzerland

Received: April 30, 2010; Revised Manuscript Received: August 22, 2010

Grazing incidence small-angle X-ray scattering (GISAXS) is used for nondestructive characterization of colloidal crystals of different numbers of hexagonally dense packed layers fabricated by convective self-assembly. Whereas small crystallites with random orientation were obtained in case of monolayers, the scattering data obtained from multilayer samples revealed colloidal domains over areas of a few centimeters where the single crystalline domains are mainly aligned along the growth direction. The data indicates an increasing degree of self-organization going from monolayers to multilayers. Within the multilayer samples, the stacking sequence of the hexagonally packed layers is evaluated using a numerical model for fitting the X-ray scattering data containing the stacking parameter, a . Compared with an expected complete random stacking with $a = 0.5$, the fitted stacking parameter, $a = 0.63 \pm 0.01$, averaged over a sample area of about 1 mm² indicates a preference for a cubic stacking sequence. This value is smaller than reported by various local probe techniques.

1. Introduction

Colloidal crystals present a promising bottom-up approach toward the fabrication of photonic materials with a complete photonic band gap. The main challenge of the approach is the quality of the colloidal crystals as the domain size, the density of voids, the crystallographic order, the number of layers, and the flatness of the surface define the optical properties of the material. Adequate characterization methods are therefore imperative to control the fabrication processes.

The surface of colloidal crystals is typically probed by SEM and AFM, techniques that provide local information about domain sizes and domain orientations.^{1–10} Similar information can be gained by laser diffraction^{4,6,11,12} or small-angle X-ray scattering,^{13–18} in which the crystal is probed in transmission mode. The internal structure of colloidal multilayers deposited on a substrate has been investigated by confocal microscopy,³ spectroscopic methods,^{3,5,19} and, to some extent, by SEM.^{2,3} The drawback of all these methods is that they provide local information, and the nondestructive characterization of the entire sample is demanding. This task can be achieved by use of X-ray techniques.

In this work, colloidal crystals were fabricated by convective self-assembly.²⁰ This technique provides uniform colloidal domains over large areas while employing comparatively simple setups. Grazing incidence small-angle X-ray scattering (GISAXS)^{21,22} was then used for the characterization of the colloidal crystals. GISAXS is a versatile tool to probe the shape, size, and positional correlation of microscopic objects located at surfaces, interfaces, or in thin films over macroscopic length scales. A schematic setup of a GISAXS experiment is displayed in Figure

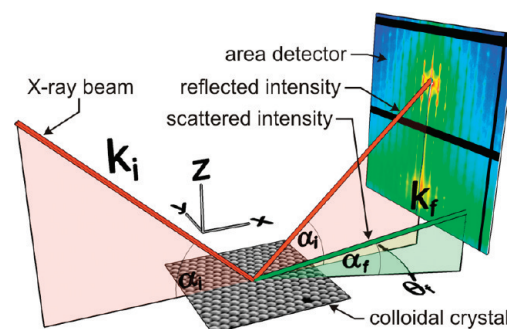


Figure 1. Schematic setup of a GISAXS experiment. A monochromatic beam with wavevector \mathbf{k}_i hits the sample with an incident angle α_i . This angle is typically close to the angle of total external reflection of the X-rays from the sample. The scattered intensity, \mathbf{k}_f , is usually measured with an area detector. The distance between sample and detector varies depending on the required resolution. For the sake of clarity, angles and distances are strongly exaggerated with respect to a real experiment.

1. A monochromatic X-ray beam hits the sample under a grazing incident angle, α_i . This angle is typically close to the angle of total external reflection of the X-rays from the top layer film. Scattering intensities are measured both at specular (in-plane angle $\theta_f = 0$) and off-specular positions ($\theta_f > 0$). As a consequence, one gains information on the structure of the sample both parallel to the substrate surface (x – y plane) and perpendicular to it (z direction).

A simulation tool was developed for the modeling of the GISAXS data measured from colloidal multilayers. It includes reflection and refraction effects arising for experiments at grazing scattering angles. The implemented model was used to fit the scattering data.

2. Materials and Methods

2.1. Sample Preparation and Characterization. Aqueous suspensions of polystyrene particles with diameters in the range

* Corresponding author. E-mail: Thomas.geue@psi.ch.

[†] Laboratory for Neutron Scattering, ETH Zurich and Paul Scherrer Institut.

[‡] Research Department of Synchrotron Radiation and Nanotechnology, Paul Scherrer Institut.

[§] Solid State Physics Group, University of Siegen.

[⊥] Laboratory for Surface Science and Technology, ETH Zurich.

277–740 nm and a nearly monodisperse size distribution (<3% coefficient of variation) were purchased from commercial suppliers (microParticles GmbH or Thermo Fisher Scientific). The colloidal dispersion was diluted to a concentration of 1 wt % using deionized water. Colloidal crystals were formed by “drag coating”.⁶ A droplet of colloidal dispersion was trapped between two glass plates. By moving one of the slides, a meniscus was dragged along the substrate. The setup was built as described elsewhere.⁸ The spreader plate was tilted 30° away from the horizontal plane. In the case of the 277 nm particles, translational velocities of 2 and 6 $\mu\text{m/s}$ resulted in colloidal crystals with one and seven layers, accordingly. For these cases, the temperature of the sample stage was set to 15 °C. Relative humidity was 18%, and the ambient temperature was ~ 20 °C. Bisected microscopy slides (Marienfeld) were used as substrates. The slides were cleaned by consecutive sonication in toluene, isopropyl alcohol, acetone, and deionized water (Millipore). The surface of the fabricated colloidal crystals were investigated by an AFM (Dimension 3100, Digital Instruments) operated in intermittent contact mode. Both surface and cross sections of the crystals were probed by SEM (SUPRA 55VP, Zeiss). It was typically operated at an electron energy of 1 keV, and secondary electrons were detected in-lens.

The surface of the fabricated colloidal crystals were investigated by an AFM (Dimension 3100, Digital Instruments) operated in intermittent contact mode. Both surface and cross sections of the crystals were probed by SEM (SUPRA 55VP, Zeiss), typically operated at an electron energy of 1 keV, and secondary electrons were detected in-lens.

All GISAXS experiments were performed at the cSAXS beamline located at the Swiss Light Source (Paul Scherrer Institute, Villigen, Switzerland)²³ using photon energies of 8.7 or 11.7 keV. The X-ray beam was focused on the detector plane on a size of approximately one pixel ($172 \times 172 \mu\text{m}^2$). The beam diameter at the sample position was around $1 \times 1 \text{ mm}^2$. A 7-m-long flight tube with an entrance window of $\sim 5\text{--}7\text{-}\mu\text{m}$ -thick mica was inserted between the sample and the PILATUS 2M^{24,25} detector. Depending on the experiment, the exit window consisted of a $\sim 13\text{-}\mu\text{m}$ -thick Kapton or a $\sim 350\text{-}\mu\text{m}$ -thick Mylar foil. The flight tube was evacuated or filled with helium.

3. Theory for the Numerical Fitting of the Scattering Data

To the best of our knowledge, none of the available tools^{26–28} for simulation of GISAXS data has the option to *fit* scattering data from a thin film comprising a three-dimensional crystalline arrangement. To analyze the GISAXS data collected from colloidal multilayers, a tool was implemented on the basis of IDL (ITT VIS) programming language being available from the corresponding author upon request. In the following, the employed theory and approximations are shortly discussed.

GISAXS experiments are described in terms of the distorted wave Born approximation²⁹ taking reflection and refraction effects at shallow incident angles into account. For the fitting of X-ray scattering, we have considered four out of 16 terms. A thin film with thickness d on top of a substrate was chosen as the unperturbed system. The intensity I scattered from small perturbations in the film into the solid angle $\Delta\Omega r^2$ was calculated by.^{30,31}

$$I = \frac{1}{16\pi^2} \frac{1 - e^{-2\text{Im}(Q_z)d}}{2(Q_z)} \times [|T_i T_f F(Q_x, Q_y, \text{Re}(Q_{1,z}))|^2 + |T_i R_f F(Q_x, Q_y, \text{Re}(Q_{2,z}))|^2 + |R_i T_f F(Q_x, Q_y, \text{Re}(Q_{3,z}))|^2 + |R_i R_f F(Q_x, Q_y, \text{Re}(Q_{4,z}))|^2] \quad (1)$$

T_i , T_f , R_i and R_f denote the amplitude reflectivity and transmission coefficients in the colloidal layer. They can be calculated using, e.g., Parratt’s recursive method.³² The following notations were used for the components of the scattering vector $\mathbf{Q} = \mathbf{k}_f - \mathbf{k}_i$ in the colloidal layer: $Q_x = k_{x,f} - k_{x,i}$, $Q_y = k_{y,f} - k_{y,i}$, $Q_{1,z} = k_{z,f} - k_{z,i}$, $Q_{2,z} = -k_{z,f} - k_{z,i}$, $Q_{3,z} = k_{z,f} + k_{z,i}$, $Q_{4,z} = k_{z,f} - k_{z,i}$. The terms $F(Q_x, Q_y, \text{Re}(Q_{i,z}))$ in eq 1 correspond to the scattering amplitudes of the colloidal crystal in the Born approximation with different wave vector transfers. In the numerical implementation, the absolute squares of these terms were calculated under the assumption of the decoupling approximation,²² according to

$$|F(Q_x, Q_y, \text{Re}(Q_{i,z}))|^2 = \underbrace{r_0^2 N \cdot \left[\langle |f_m|^2 \rangle - \langle f_m \rangle^2 \right]}_{I_{\text{incoh}}} e^{-W(\mathbf{Q})} + \underbrace{r_0^2 \langle f_m \rangle^2 e^{-W(\mathbf{Q})} \left\langle \left| \sum_{m=1}^N e^{i\mathbf{Q}\mathbf{r}_m} \right|^2 \right\rangle}_{I_{\text{coh}}} \quad (2)$$

where I_{incoh} and I_{coh} are the incoherent and coherent scattering of a crystalline lattice, respectively. N corresponds to the number of unit cells of the crystal contributing to the scattered intensity, and r_0 is the Thomson scattering length. The f_m denote the form factor of the colloidal particles. Their shape was approximated by a sphere with radius r_m :

$$f_m(\mathbf{Q}, r_m) = 3 \frac{\sin(Qr_m) - Qr_m \cos(Qr_m)}{(Qr_m)^3} \quad (3)$$

The brackets enclosing f_m in eq 2 denote averaging over the particle size distribution. Accounting for monodispersity, a Gaussian distribution was used for data fitting. The term $e^{-W(\mathbf{Q})}$ in eq stands for the Debye–Waller factor with $W(\mathbf{Q}) = \mathbf{Q}^T \mathbf{B} \mathbf{Q}$, and \mathbf{B} is the tensor of the standard deviations of the particle positions from the ideal lattice.

A colloidal crystal consists typically of hexagonally close packed layers (parallel to the x – y plane) that are stacked on top of each other in the two possible 3-fold coordinated sites of the layer beneath. The multilayers are therefore well-ordered along the planes, but along the z direction, the stacking can be irregular, leading to a mixture of a hexagonal close packed (hcp) and face centered cubic (fcc) crystalline order. This stacking sequence is described by a structure factor, $S_L(\mathbf{Q})$ calculated by the analytical function for the layered systems with disordered stacking derived in.³³

$$S_L(\mathbf{Q}) = \langle |L(\mathbf{Q})|^2 \rangle \frac{A}{B} \quad (4)$$

where

$$A = a(1 - a) \left[1 - \cos\left(2\pi \frac{2k - h}{3}\right) \right]$$

$$B = 2(1 - 2a)[1 - \cos^2(2\pi l)] + 3a^2 - 4a^2(-1)^h \times \cos\left(2\pi \frac{2k - h}{6}\right) \cos(2\pi l) + a^2 \cos\left(2\pi \frac{2k - h}{3}\right)$$

$|L(\mathbf{Q})|^2$ in eq 4 is the scattering intensity from a single layer (i.e., the layer form factor of a hexagonal plane). It was assumed that all layers scatter identically. The structure factor, $S_L(\mathbf{Q})$, can therefore be understood as the product of the layer form factor multiplied by a term describing the stacking of the individual layers. The second term modifies the intensity of the scattering rods in the Q_z direction. The Miller indices h, k, l denote the components of the scattering vector $\mathbf{Q} = h\mathbf{a}_1^* + k\mathbf{a}_2^* + l\mathbf{a}_3^*$ expressed as a linear combination of the reciprocal lattice vectors

$$\mathbf{a}_1^* = \frac{2\pi}{d_{\text{col}}} \left(\mathbf{x}^* - \sqrt{\frac{1}{3}} \mathbf{y}^* \right), \mathbf{a}_2^* = \frac{2\pi}{d_{\text{col}}} \sqrt{\frac{4}{3}} \mathbf{y}^*, \mathbf{a}_3^* = \frac{2\pi}{d_{\text{col}}} \sqrt{\frac{3}{2}} \mathbf{z}^* \quad (5)$$

as illustrated in Figure 2. d_{col} corresponds thereby to the distance between the scattering centers in the hexagonal planes in real space; and $\mathbf{x}^*, \mathbf{y}^*, \mathbf{z}^*$ are the unit vectors in reciprocal space. The parameter a introduced in eq 4 is called the stacking probability. It denotes the likelihood that two consecutive hexagonal layers are stacked using one and the same translation

operation. $a = 1$ corresponds accordingly to a pure fcc stacking; $a = 0$, to a pure hcp stacking; and $a = 0.5$, to a complete random stacking. The stacking probability is used to characterize the irregular stacking of the colloidal layers in the z direction. The stacking probability is discussed more extensively in ref 33 and the references therein. In Figure 2a, the modulation of the scattered intensity along \mathbf{z}^* (\mathbf{a}_3^* , i.e., along the Miller index l) was plotted for different values of a .

Whenever

$$\left(\frac{h+k}{3}\right) \in \{0, 1, -1, 2, -2, \dots\} \quad \text{and} \quad \left(\frac{2k-h}{3}\right) \in \{0, 1, -1, 2, -2, \dots\} \quad (6)$$

eq 4 can be simplified,³³ and one obtains

$$S_L(\mathbf{Q}) = \left| L(\mathbf{Q}) \right|^2 \left| \frac{\sin(\pi l L)}{\sin(\pi l)} \right|^2 \quad (7)$$

the case of Bragg scattering from a stack of L planes with peaks at $l = 1, 2, \dots$. The scattering at these positions is independent of the stacking probability. Figure 2b is a schematic representation of a two-dimensional hcp plane in reciprocal space. Equation 6 is fulfilled for the positions marked with the open circles.

For the setup used in this work at the cSAXS beamline, the experimental resolution was determined mainly by the pixel size of the Pilatus detector ($172 \mu\text{m} \times 172 \mu\text{m}$). No spread in the angles and the wavelength were incorporated in the numerical implementation to fit the scattering data.

4. Results and Discussion

Figure 3 shows results from SEM and AFM investigations of colloidal crystals. Convective self-assembly allowed the fabrication of crystals with an almost homogeneous number of layers across areas of $1\text{--}2 \text{ cm}^2$. The arrows on the AFM micrographs in Figure 3a, b indicate the direction of translation of the meniscus of colloidal dispersion over the glass substrate during the formation process. This direction will be further referred to as the *growth direction* because the crystal has developed in this direction.

Locally, the investigations revealed an almost perfect hexagonal arrangement of the colloidal particles. For distances exceeding ~ 30 particle diameters, the order starts to slowly break down due to inclusion of various defects. In the case of colloidal multilayers, cracks extending over several colloidal diameters are observed. From the fact that the boundaries of the cracks match each other exactly, one concludes that the domains did not nucleate individually, but have cracked after the formation process. These observations have been explained by volume shrinkage of the film during drying and the action of capillary forces.^{2,3,34} From SEM and AFM investigations at different positions on the colloidal crystals, it was found that all probed domains of the multilayers exhibit an almost identical orientation. The colloidal particles are aligned along the direction of growth of the colloidal crystal. The correlation between the growth direction and the domain orientation of crystals fabricated with convective self-assembly has also been observed in refs 35 and 36. No preferential orientation of the domains was observed in the case of the colloidal monolayers.

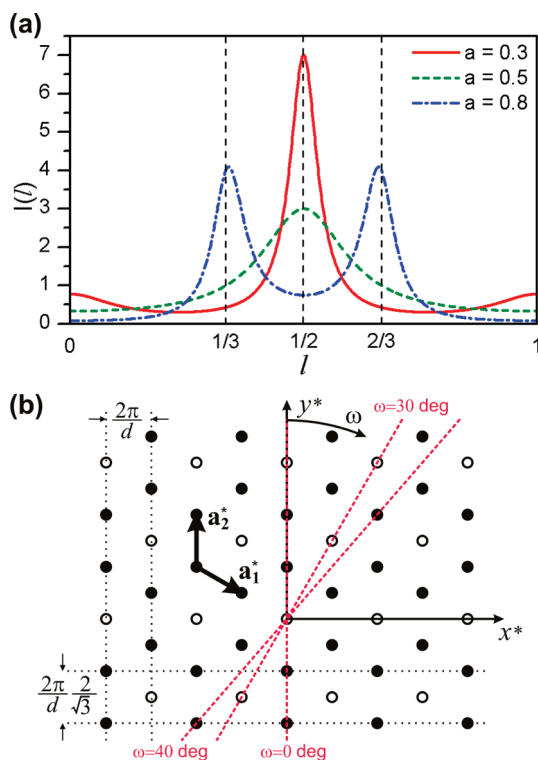


Figure 2. (a) Relative dependence of the scattering intensity along \mathbf{z}^* (\mathbf{a}_3^*) on the stacking probability, a . The curves were calculated according to eq 4. $a = 0.5$ corresponds to a completely random stacking. (b) Schematic representation of the two-dimensional hcp plane in reciprocal space. Equation 6 is fulfilled for the positions marked with the open circles. At these positions, the scattering rods along \mathbf{z}^* (\mathbf{a}_3^*) are independent of the stacking probability, a . The rest of the scattering rods exhibits the strong dependence on a as depicted in part a. The red dotted lines illustrate the orientation of the scattering patterns displayed in Figure 4.

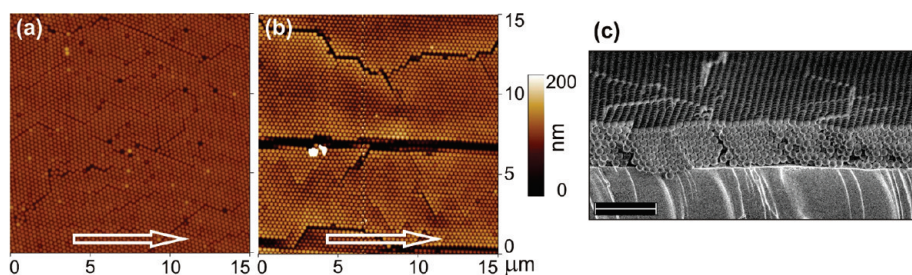


Figure 3. AFM micrographs of a colloidal monolayer (a) and a colloidal multilayer (b) consisting of particles with a diameter of 277 nm. (c) Cross-sectional view through the same multilayer as in part a, taken by SEM. The crystal is fractured perpendicular to the growth direction. The scale bar corresponds to 2 μm .

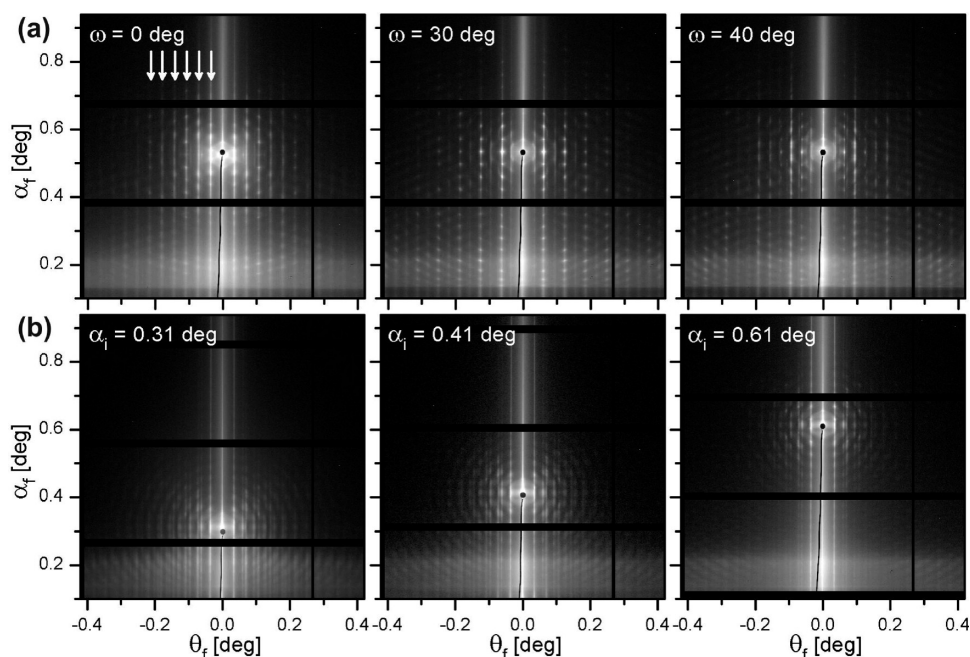


Figure 4. (a) Scattering patterns collected from a crystal consisting of seven layers of particles with a diameter of 277 nm. The scattering patterns were measured at $\alpha_i = 0.53^\circ$ but at varying ω . The corresponding sections through reciprocal space are indicated in Figure 2b. The arrows in the left Figure mark the positions where sections have been extracted for the out of plane evaluation. The displayed scattering patterns are an average over 11 exposures, covering an ω -range of 1° . (b) Scattering pattern from a colloidal monolayer of particles with a diameter of 277 nm measured at different incident angles. The scattering patterns correspond to an average over 31 exposures, covering an ω -range of 3° . The averaging was done uniquely for a distinct representation of the scattering patterns. A further description is given in the text.

Figure 4 displays GISAXS patterns collected from colloidal crystals. The crystals were formed by particles with a diameter of 277 nm. In the case of Figure 4a, the sample consisted of seven stacked monolayers. The corresponding scattering patterns were collected at identical incident angles, $\alpha_i = 0.53^\circ$, but different azimuthal orientation, ω . The angle ω denotes the rotation of the sample around its surface normal, where the angle $\omega = 0$ defines the orientation where the growth direction is parallel to the X-ray beam. The scattering rods parallel to α_f exhibit an extensive number of peaks evidencing the three-dimensional colloidal arrangement. Figure 4b corresponds to GISAXS patterns measured from a colloidal monolayer. The scattering patterns were measured at different incident angles but an identical azimuthal orientation. The concentric intensity circles around the position of the reflected beam are generated by the colloidal form factor (see eq 3).

The black “bars” appearing on all scattering patterns originate from insensitive parts between the modules of the Pilatus detector.^{24,25} The high intensity of the reflected beam was absorbed by a beam stop that was inserted from below. The intensity range from $\alpha_f \approx 0.14^\circ$ up to $\alpha_f \approx 0.22^\circ$ is affected by dynamical scattering effects that are dominant close to the angle of total external reflection and will be further referred as the

Yoneda band in text. The position of the upper and lower limit of the Yoneda band is defined by the critical angles of the glass substrate and the colloidal particles, respectively. The detected intensity decreases rapidly below the Yoneda band (not shown in Figure 4). No scattering intensity was measured below the sample horizon for any sample.

The axes α_f and θ_f are defined in Figure 1. In a first approximation, the α_f -axis is parallel to \mathbf{z}^* (\mathbf{a}_3^*), and the θ_f -axis is parallel to the \mathbf{x}^* – \mathbf{y}^* plane. The direction of the θ_f axes of the scattering patterns in Figure 4a can be attributed to (010) at $\omega = 0^\circ$, (120) at $\omega = 30^\circ$, and (230) at $\omega = 40^\circ$ with the coordinate system as defined in eq 5 and Figure 2b.

4.1. In-Plane Evaluation of the GISAXS Data. The calculated resolution in the θ_f direction amounts to $\Delta Q_y = 0.0013 \text{ nm}^{-1}$ for the cSAXS beamline. The maximally measurable correlation length corresponded, therefore, to 4.8 μm , that is, around 17 particle diameters in the case of the 277 nm colloids. Therefore, no significant information on the domain sizes can be gained in the case of these large particles.

To probe the *in-plane* arrangement of the colloidal particles, the samples were turned around ω , and scattering patterns were measured every 0.1° in an ω range of 100° at constant α_i . The individual patterns were integrated over α_f between the lower

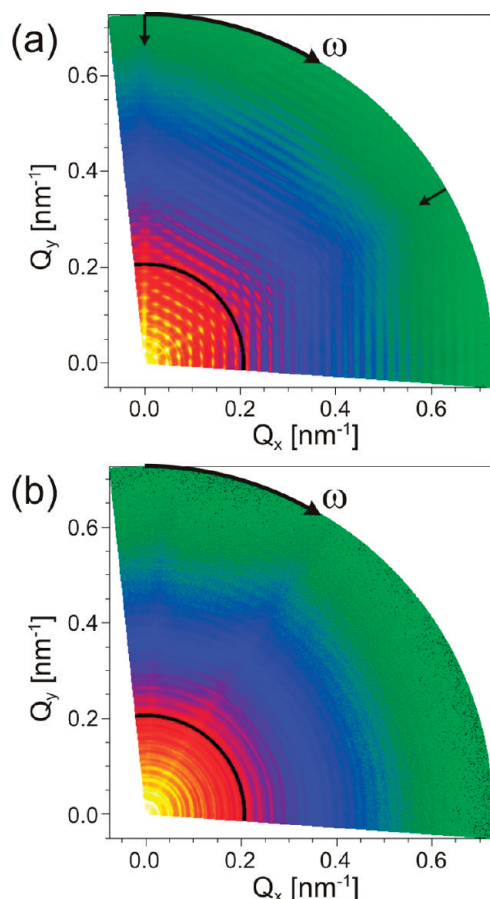


Figure 5. (a) In-plane evaluation of the GISAXS data of a colloidal multilayer consisting of seven layers of colloids with a diameter of 277 nm. The black segment in the graph is caused by the gap between two detector modules. (b) In-plane evaluation of a monolayer consisting of particles with a diameter of 277 nm.

limit of the Yoneda band and the position of the reflected beam. The resulting intensities were plotted in a polar graph in which the angle and radial position of each intensity element was defined by the corresponding sample orientation, ω , and the distance to the specular direction, θ_f , respectively. Resulting graphs can be seen in Figure 5. Due to the symmetry of the pattern with respect to θ_f , only positive θ_f values are displayed. The angular coordinates were transformed to the components of the scattering vector Q_x and Q_y , assuming that the basis vectors of reciprocal space are fixed to the sample; that is, Q_x is always oriented parallel to the growth direction, and Q_y is perpendicular to it.

Scattering data for Figure 5a was measured at $\alpha_i = 0.329 \pm 0.005^\circ$, and the data were integrated for $0.14^\circ \leq \alpha_i \leq 0.36^\circ$. The figure gives clear evidence of hexagonal arrangement of the colloids on the sample. This ordering is indicated by streaks of intensity along the radial direction separated by an ω angle of 60° from each other. The data originates from the same sample (composed of seven colloidal layers) as selected for Figure 4a. Considering the grazing incidence angle and the vertical beam size of almost 1 mm at sample position, the beam footprint is more than 10 cm long, and the complete sample is illuminated. It follows that the domains on the complete self-assembled sample are likewise oriented. The similar observation made at other multilayers is in good agreement with SEM and AFM results.

Figure 5b corresponds to the in-plane evaluation of the scattering data for the colloidal monolayer shown in Figure 4b.

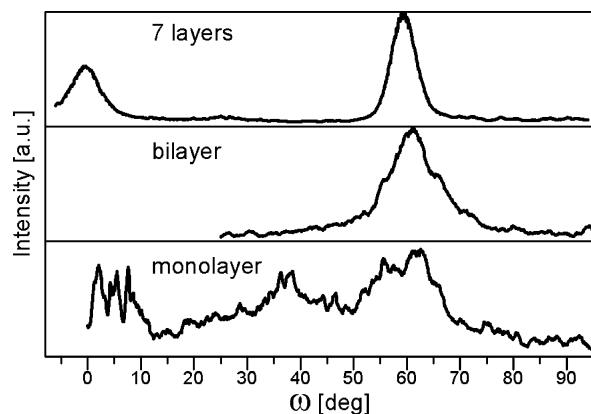


Figure 6. Sections along ω extracted from graphs as shown in Figure 5 while holding $Q_{||} = (Q_x^2 + Q_y^2)^{1/2}$ constant. The corresponding $Q_{||}$ value for each of the three displayed ω scans was chosen such that the section came to rest on a peak when crossing the directions at $\omega = 0^\circ$ and 60° , marked with an arrow in Figure 5a. The three displayed cases correspond to crystals consisting of seven, two, and one colloidal layer. The curves were independently scaled.

The scattering data were measured at $\alpha_i = 0.314 \pm 0.005^\circ$ and integrated for $0.16^\circ \leq \alpha_i \leq 0.37^\circ$. The concentric circles indicate that the domains have a random orientation in the x - y plane and show a powder-like scattering behavior. The position of the circles cannot be explained by a simple form factor of a sphere. The streaks seen along the radial direction for various ω positions cannot be associated with a certain in-plane ordering of the spheres. The result from the GISAXS data confirms the AFM investigations on the monolayer where a random orientation of the domains was found, as well.

Figure 6 shows line scans along ω extracted from Figure 5 where the absolute value of the in-plane scattering vector, $Q_{||} = (Q_x^2 + Q_y^2)^{1/2}$, is kept constant. The three radial scans correspond to crystals consisting of seven, two, and one colloidal layer. The curves are individually scaled in intensity. In the case of the monolayer, the intensity distribution does not exhibit any distinct dependence on ω . The variations in intensity can be attributed to changes in the illuminated part on the sample. These variations are already visible in Figure 5b. With two layers, a broad peak with a fwhm of $7.5 \pm 2.5^\circ$ develops, and this peak is even more pronounced for the crystal with seven layers, where the fwhm amounts to $4.4 \pm 0.9^\circ$.

From the evaluation of in-plane ordering, we conclude that the transition from a convectively self-assembled monolayer toward a multilayer goes in parallel with the development of a directed self-assembly of particles. In the case of monolayers, the assembly mechanism is well studied.^{37–40} It is explained by particle aggregation due to capillary immersion forces. These forces start to act as colloidal particles protruding from thin water films. In the case of multilayers, the process is understood qualitatively only. No mechanism is identified so far that could explain in detail how three-dimensional, close packed structures of colloidal spheres emerge. First theoretical considerations have identified two mechanisms that could lead to the specific stacking order of the colloidal particles:⁴¹ Both solvent flow through the pore space between the already packed colloids and a flow parallel to the surface of a hexagonal packed layer can lead to a selective deposition of particles. It can be hypothesized that the strength of the solvent flow also plays a role in the macroscopic alignment of the domains.

4.2. Out of Plane Evaluation of the GISAXS Data. Vertical stacking of the colloidal layers can be obtained from *out of plane* GISAXS data. The corresponding evaluation is demonstrated

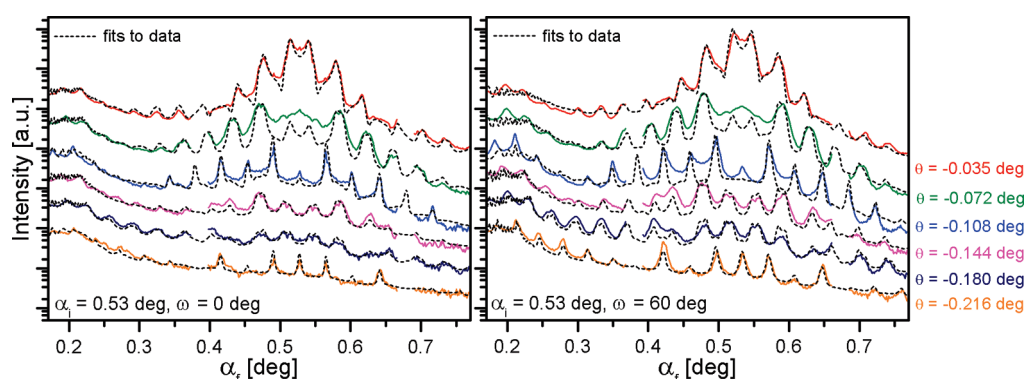


Figure 7. Fits (black dashed lines) to GISAXS data (colored solid lines) of crystal consisting of seven layers of particles with a diameter of 277 nm. The sections were extracted from the scattering patterns at the position of the scattering rods, as indicated in Figure 4a. They correspond to an average over 30 individual scattering patterns collected in an ω range of 3° . Practically, no change could be detected in the corresponding scattering patterns. The intensity scale is logarithmic. The curves are vertically displaced for better visibility.

for the sample consisting of seven layers of 277 nm particles already discussed previously. To do this, line scans for constant θ_f were extracted from 2D GISAXS data as marked by arrows in Figure 4a. Examples of line cuts are displayed in Figure 7 for $\alpha_i = 0.53^\circ$ and $\omega = 0^\circ$ and 60° , respectively.

The extracted line scans differ in peak shapes and peak positions. The first, second, fourth, and fifth curves, counted from top, exhibit broad, double peaks that are located between the peaks of the third and sixth curves. The latter peaks are rather sharp. The experimental scattering patterns associated with the line scans correspond approximately to planes in reciprocal space that intersect the hexagonal plane displayed in Figure 2b at the position of the red dotted line marked with $\omega = 0$. (The line for $\omega = 60^\circ$ is not marked, but is equivalent in symmetry to the position $\omega = 0^\circ$.) By following this red line in Figure 2b, one finds a succession of two positions that are sensitive to the stacking of the hexagonal layers (full circles), followed by one position that exhibits simple Bragg-like reflection (open circle) (see eq 7). The first, second, fourth, and fifth curves in Figure 7 correspond, therefore, to scattering rods that are sensitive to the stacking probability, whereas the third and sixth curves display Bragg-like reflections. The different peak shapes and positions can be understood accordingly.

The model introduced in section 3 was used to fit the lines scans and accordingly to make an estimate for the stacking probability. The line scans shown in Figure 7 and additional ones taken at different incident angles, $0.33^\circ \leq \alpha_i \leq 0.63^\circ$, and sample orientations, $\omega = 0^\circ$ and 60° , were thereby fitted to the model. The visual comparison between experimental data and resulting fits does not show significant differences. In addition, the same fit parameters were obtained for the different α_i 's and ω 's. This is in accordance with the expectation that the complete thickness of the multilayer film is probed for all α_i 's used. The obtained stacking probability amounts to $a \approx 0.63 \pm 0.01$. This probability is clearly above the value $a = 0.5$ that refers to completely random stacking and indicates a tendency toward fcc ordering of the hexagonally stacked layers. As a fingerprint of this a -value, we found that the double peaks on the scattering rods being sensitive to the stacking sequence appear only from a value $a \geq 0.61$ on.

Compared with earlier studies that found fcc stacking with just a few stacking faults in samples fabricated with convective self-assembly,^{3,5,41} our stacking parameter is rather low. This difference is due to the different methods used for the characterization. Whereas in earlier studies, single domains were inspected using local probes, such as confocal microscopy³ and spectroscopic methods,^{3,5,19} GISAXS provides a stacking prob-

ability that is a statistical average over the complete volume of the sample illuminated by the X-ray beam; that is, over several square millimeters. To our knowledge, GISAXS is the only technique so far that provides this large-area information on the stacking of the hexagonally packed monolayers perpendicular to the substrate surface in a destruction-free manner. Different fabrication parameters for the colloidal self-assembly in earlier studies could be a further reason for the differing stacking probability.⁴¹

5. Conclusions

In the presented investigation, we show that GISAXS can be well used to characterize colloidal crystals fabricated by convective self-assembly. GISAXS data demonstrates that the investigated colloidal multilayers have an orientation similar to the domains over the complete sample and are aligned along the growth direction. The same preferential domain orientation was also observed for bilayers but relaxed with respect to the multilayers. In contrast to this, monolayers exhibit a random orientation of the domains. Methodically, the approach presented for evaluation of the in-plane scattering data shows that GISAXS is an ideal tool to detect the exact degree of the domain alignment of 3D colloidal crystals. This is in advantage to SEM and AFM, where this information can be accessed only by a laborious evaluation of large numbers of individual micrographs.

The stacking of the hexagonally ordered layers of a colloidal multilayer (seven layers) was evaluated by fitting the corresponding GISAXS data with a numerical model. The extracted stacking probability of $a = 0.63 \pm 0.01$ indicates a tendency toward fcc stacking. Compared with earlier studies, the relatively low value can be understood by the fact that previous studies investigated the crystals on a local basis, whereas the information obtained by GISAXS is a statistical average over several square millimeters. To our knowledge, GISAXS is the only method so far that can provide statistical relevant information on the stacking of 3D hexagonally packed monolayers perpendicular to the substrate surface in a destruction-free manner.

Acknowledgment. The authors thank T. Kraus (ETH Zurich) and W. Steurer (ETH Zurich) for their support and very helpful inputs. AFM and SEM measurements were performed in the Laboratory for Micro- and Nanotechnology at the Paul Scherrer Institute. This work is supported by the Swiss National Funds Grant No. 200021-107796.

References and Notes

- (1) Bertone, J. F.; Jiang, P.; Hwang, K. S.; Mittleman, D. M.; Colvin, V. L. *Phys. Rev. Lett.* **1999**, *83*, 300.

- (2) Jiang, P.; Bertone, J. F.; Hwang, K. S.; Colvin, V. L. *Chem. Mater.* **1999**, *11*, 2132.
- (3) Gu, Z. Z.; Fujishima, A.; Sato, O. *Chem. Mater.* **2002**, *14*, 760.
- (4) Goldenberg, L. M.; Wagner, J.; Stumpe, J.; Paulke, B. R.; Gornitz, E. *Langmuir* **2002**, *18*, 3319.
- (5) Vlasov, Y. A.; Bo, X. Z.; Sturm, J. C.; Norris, D. J. *Nature* **2001**, *414*, 289.
- (6) Prevo, B. G.; Velez, O. D. *Langmuir* **2004**, *20*, 2099.
- (7) Zhou, Z.; Zhao, X. S. *Langmuir* **2004**, *20*, 1524.
- (8) Malaquin, L.; Kraus, T.; Schmid, H.; Delamarche, E.; Wolf, H. *Langmuir* **2007**, *23*, 11513.
- (9) Mayoral, R.; Requena, J.; Moya, J. S.; Lopez, C.; Cintas, A.; Miguez, H.; Meseguer, F.; Vazquez, L.; Holgado, M.; Blanco, A. *Adv. Mater.* **1997**, *9*, 257.
- (10) Rogach, A. L.; Kotov, N. A.; Koktysh, D. S.; Ostrander, J. W.; Ragoisha, G. A. *Chem. Mater.* **2000**, *12*, 2721.
- (11) Allard, M.; Sargent, E. H.; Lewis, P. C.; Kumacheva, E. *Adv. Mater.* **2004**, *16*, 1360.
- (12) Amos, R. M.; Rarity, J. G.; Tapster, P. R.; Shepherd, T. J.; Kitson, S. C. *Phys. Rev. E* **2000**, *61*, 2929.
- (13) Petukhov, A. V.; Aarts, D.; Dolbnya, I. P.; de Hoog, E. H. A.; Kassapidou, K.; Vroege, G. J.; Bras, W.; Lekkerkerker, H. N. W. *Phys. Rev. Lett.* **2002**, *88*.
- (14) Petukhov, A. V.; Dolbnya, I. P.; Aarts, D.; Vroege, G. J. *Phys. Rev. E* **2004**, *69*.
- (15) Petukhov, A. V.; Dolbnya, I. P.; Aarts, D.; Vroege, G. J.; Lekkerkerker, H. N. W. *Phys. Rev. Lett.* **2003**, *90*.
- (16) Petukhov, A. V.; Thijssen, J. H. J.; Hart, D. C.; Imhof, A.; van Blaaderen, A.; Dolbnya, I. P.; Snigirev, A.; Moussaid, A.; Snigireva, I. *J. Appl. Crystallogr.* **2006**, *39*, 137.
- (17) Thijssen, J. H. J.; Petukhov, A. V.; Hart, D. C.; Imhof, A.; van der Werf, C. H. M.; Schropp, R. E. I.; van Blaaderen, A. *Adv. Mater.* **2006**, *18*, 1662.
- (18) Vos, W. L.; Megens, M.; vanKats, C. M.; Bosecke, P. *Langmuir* **1997**, *13*, 6004.
- (19) Checoury, X.; Enoch, S.; López, C.; Blanco, A. *Appl. Phys. Lett.* **2007**, *90*, 161131.
- (20) Dimitrov, A. S.; Nagayama, K. *Chem. Phys. Lett.* **1995**, *243*, 462.
- (21) Muller-Buschbaum, P. *Anal. Bioanal. Chem.* **2003**, *376*, 3.
- (22) Renaud, G.; Lazzari, R.; Leroy, F. *Surf. Sci. Rep.* **2009**, *64*, 255.
- (23) cSAXS. Webpage cSAXS beamline.
- (24) Bech, M.; Bunk, O.; David, C.; Kraft, P.; Brönnimann, C.; Eikenberry, E. F.; Pfeiffer, F. *Appl. Radiat. Isotopes* **2008**, *66*, 474.
- (25) Kraft, P.; Bergamaschi, A.; Broennimann, C.; Dinapoli, R.; Eikenberry, E. F.; Henrich, B.; Johnson, I.; Mozzanica, A.; Schleputz, C. M.; Willmott, P. R.; Schmitt, B. *J. Synchrotron Radiat.* **2009**, *16*, 368.
- (26) Lazzari, R. *J. Appl. Crystallogr.* **2002**, *35*, 406.
- (27) Tate, M. P.; Hillhouse, H. W. *J. Physical Chem. C* **2007**, *111*, 7645.
- (28) Tate, M. P.; Urade, V. N.; Kowalski, J. D.; Wei, T. C.; Hamilton, B. D.; Eggiman, B. W.; Hillhouse, H. W. *J. Phys. Chem. B* **2006**, *110*, 9882.
- (29) Pietsch, U.; Holý, V.; Baumbach, T. *High-resolution X-ray scattering from thin films to lateral nanostructures*, 2nd ed. ed.; Springer Verlag: New York, 2004.
- (30) Lee, B.; Park, I.; Yoon, J.; Park, S.; Kim, J.; Kim, K. W.; Chang, T.; Ree, M. *Macromolecules* **2005**, *38*, 4311.
- (31) Lee, B.; Yoon, J.; Oh, W.; Hwang, Y.; Heo, K.; Jin, K. S.; Kim, J.; Kim, K. W.; Ree, M. *Macromolecules* **2005**, *38*, 3395.
- (32) Parratt, L. G. *Phys. Rev.* **1954**, *95*, 359.
- (33) Loose, W.; Ackerson, B. *J. Chem. Phys.* **1994**, *101*, 7211.
- (34) Teh, L. K.; Tan, N. K.; Wong, C. C.; Li, S. *Appl. Phys. A: Mater. Sci. Process.* **2005**, *81*, 1399.
- (35) Galisteo-López, J. F.; Palacios-Lidón, E.; Castillo-Martínez, E.; López, C. *Phys. Rev. B* **2003**, *68*, 115109.
- (36) Zhang, J.; Alsayed, A.; Lin, K. H.; Sanyal, S.; Zhang, F.; Pao, W. J.; Balagurusamy, V. S. K.; Heiney, P. A.; Yodh, A. G. *Appl. Phys. Lett.* **2002**, *81*, 3176.
- (37) Denkov, N. D.; Velez, O. D.; Kralchevsky, P. A.; Ivanov, I. B.; Yoshimura, H.; Nagayama, K. *Nature* **1993**, *361*, 26.
- (38) Denkov, N. D.; Velez, O. D.; Kralchevsky, P. A.; Ivanov, I. B.; Yoshimura, H.; Nagayama, K. *Langmuir* **1992**, *8*, 3183.
- (39) Kralchevsky, P. A.; Nagayama, K. *Langmuir* **1994**, *10*, 23.
- (40) Kralchevsky, P. A.; Paunov, V. N.; Ivanov, I. B.; Nagayama, K. *J. Colloid Interface Sci.* **1992**, *151*, 79.
- (41) Norris, D. J.; Arlinghaus, E. G.; Meng, L.; Heiny, R.; Scriven, L. E. *Adv. Mater.* **2004**, *16*, 1393.